Geophysical Fluid Dynamics

Three-dimensional internal gravity waves excited by a mountain

Contact person Hideshi Hanazaki

(Research Organization) Division of Atmospheric Environment, National Institute for Environmental Studies, Environment Agency of Japan

1.Introduction

Recent studies on the waves excited by an obstacle have revealed the basic nonlinear wave-generation mechanism. The two-dimensional internal gravity waves excited near resonance are found to be well described by the forced Boussinesq equation or the forced KdV(fKdV) equation [Grimshaw& Smyth (1986), Zhu,Wu & Yates (1986), Melville & Helfrich (1987) and Hanazaki (1992)]. Here, *resonance* means that the horizontal wind velocity is equal to the linear long-wave speed of one of the vertical internal wave modes. On the contrary, for the three-dimensional internal gravity waves, little results have been obtained. Solutions of the Green-Naghdi equations, forced KP (fKP) equation and the forced Boussinesq equations have been obtined by Ertekin,Webster & Wehausen (1986), Katsis & Akylas (1987) and Pedersen (1988). However, quantitative verification of these equations as a time-dependent weakly nonlinear model has yet to be done. In this study, we solve the time-dependent three-dimensional Navier-Stokes equations numerically.[Please see *J.Fluid Mech.*(1994) by Hanazaki for details.] For the saving of the space, we show here only the results for the resonant flow of two-layer fluid. It is shown that the waves resonantly excited by an obstacle are qualitatively described by the weakly nonlinear theory (fKP equation or its extensions) and an abnormal reflection similar to the Mach reflection occurs at the side wall.

2.Theory and the numerical method

The forced extended KP(fEKP) equation is given by

$$-\frac{1}{C_*}(A_T+\Delta A_X)+a_1AA_X+\varepsilon a_2A^2A_X+a_3A_{XXX}+\frac{1}{2}\int_{-\infty}^{X}dXA_{YY}+G_X=0.$$

where $A(X,Y,T)$ denotes the amplitude of the wave of the resonant mode. The fKP equation is obtained by neglecting the cubic nonlinear term $\varepsilon a_2A^2A_X$. For details, please see Hanazaki (1994). The computation was done in the domain of $x_{\min}\le x\le x_{\max}$, $0\le y\le y_{\max}=W$, and $h(x,y)\le z\le z_{\max}=D$, where W(=40D) is the half width of the channel, D is the channel depth. The mountain shape is given by

$$h(x,y)=h_{\max}\times\frac{1}{2}\left[1+\cos\left(\pi\left\{\left(\frac{x}{5D}\right)^2+\left(\frac{y}{10D}\right)^2\right\}^{\frac{1}{2}}\right)\right],$$

$$\text{where}\quad\left(\frac{x}{5D}\right)^2+\left(\frac{y}{10D}\right)^2\le 1.$$

and $h(x,y)=0$ elsewhere [$h_{\max}=0.1D$, see Figure 1]. The computation is done only for y>0 because we assume the symmetry of the flow against the plane of y=0. At y=W rigid walls exist. The undisturbed density distribution $\bar{\rho}(z)$ is given by

$$\bar{\rho}(z)=\frac{1}{2}\left[\bar{\rho}(0)+\bar{\rho}(D)\right]-\frac{1}{2}\left[\bar{\rho}(0)-\bar{\rho}(D)\right]\tanh\left[\frac{50(z-h_2)}{D}\right],$$

with $\bar{\rho}(D)=0.9\bar{\rho}(0)$, and $h_2=0.3D$. The Froude number is defined by F=U/C, where C is the linear long-wave speed of the fastest wave mode. We show here only the results for F=1 (exact resonance). The Reynolds number is defined by the height of the mountain is fixed to be 1000.

3.Results

In Figure 2, time development of the resonant(F=1.0) flow of a nearly two-layer fluid over topography is described. Here A(x,y,t)= A_1(x,y,t) is calculated using the horizontal velocity u(x,y,z,t). In the initial time development(Ut/D=40) the upstream waves are curved backwards [Figure 2(a)]. At around Ut/D=60, the far side end of the upstream waves reaches the side wall and it begins to be reflected. After that, the upstream waves become gradually straight crested as time proceeds. Downstream of the obstacle, flat depression is formed and it becomes longer as time proceeds. Further downstream, lee waves are generated[Figure 2(d)].

To compare this solution with the weakly nonlinear theory, the solutions of the fKP and the fEKP equation when F=1.0 (Ut/D=200) are shown in Figure 3. The over all qualitative feature agree with the solution of the fully nonlinear Navier-Stokes equations. However, there are some quantitative differences. Nearly flat depression just downstream of the obstacle(x>0, y=0), which is typical in the two-dimensional waves and also seen in the three-dimensional solution of the Navier-Stokes equations, does not appear in the solutions of the fKP and the fEKP equation. In addition, in the solution of the fKP equation[Figure 3(a)], the generation period of the upstream waves is shorter and the upstream-advancing speed is larger. Although the upstream waves have comparable amplitude, lee-wave amplitude is highly over predicted. In the solution of the fEKP equation[Figure 3(b)], the amplitude of the upstream wave is over predicted although the lee wave amplitude is smaller than the solution of the fKP equation. The generation period of the upstream wave is longer and the upstream-advancing speed is smaller than the solution of the Navier-Stokes equations. It seems that, except just upstream of the obstacle(x<0,y<20D), the fEKP equation shows better agreement with the Navier-Stokes equations

compared to the fKP equation. However, solution of the fEKP equation shows large differences just upstream of the obstaclewhere we have the most concern. Therefore, we can not say straightforwardly that the fEKP equation is a sufficiently accurate model of the phenomenon. We note that, although the comparisons are made here only for F=1.0, typical qualitative differences were the same for the other Froude numbers near resonance.

4.Conclusion

We have found that the three-dimensional waves excited by an obstacle near resonance in nearly two-layer flow are described qualitatively by the fKP or the fEKP equation. In the process of the two-dimensionalisation of the upstream wave, it was found that the abnormal reflection similar to the Mach reflection of a Boussinesq solitary wave plays an important role. The phenomenon could not be explained by the difference in the group velocity of the lateral mode of the linear wave.

References

1. R.C.Ertekin, W.C.Webster & J.V.Wehausen. *J.Fluid Mech.* **169**, 275 (1986).
2. R.H.J.Grimshaw & N.Smyth 1986 *J.Fluid Mech.* **169**, 429 (1986).
3. H.Hanazaki, *Phys.Fluids A***4**, 2230 (1992).
4. H.Hanazaki, *J.Fluid Mech.* (1994)(in press).
5. C.Katsis & T.R.Akylas *J.Fluid Mech.***177**,49 (1987).
6. W.K.Melville & K.R.Helfrich *J.Fluid Mech.* **178**, 31 (1987).
7. G.Pedersen *J.Fluid Mech.***196**, 39 (1988).
8. T.Y.Wu *J.Eng. Mech.Div. ASCE* **107**, 501 (1981).
9. J.Zhu, T.Y.Wu & G.T.Yates *Proc. 16th Symposium on Naval Hydrodyn.* (1986).

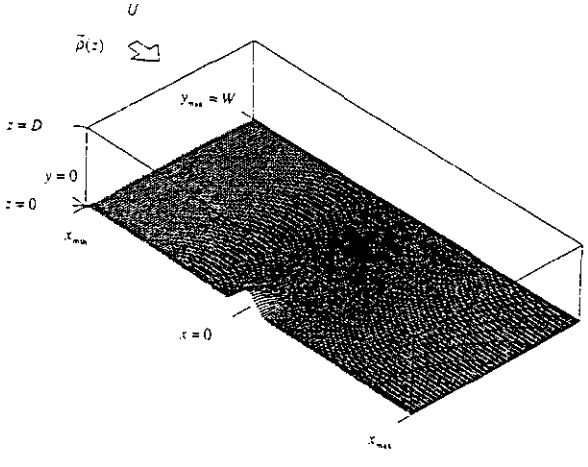

Figure 1. Schematical view of the flow geometry.

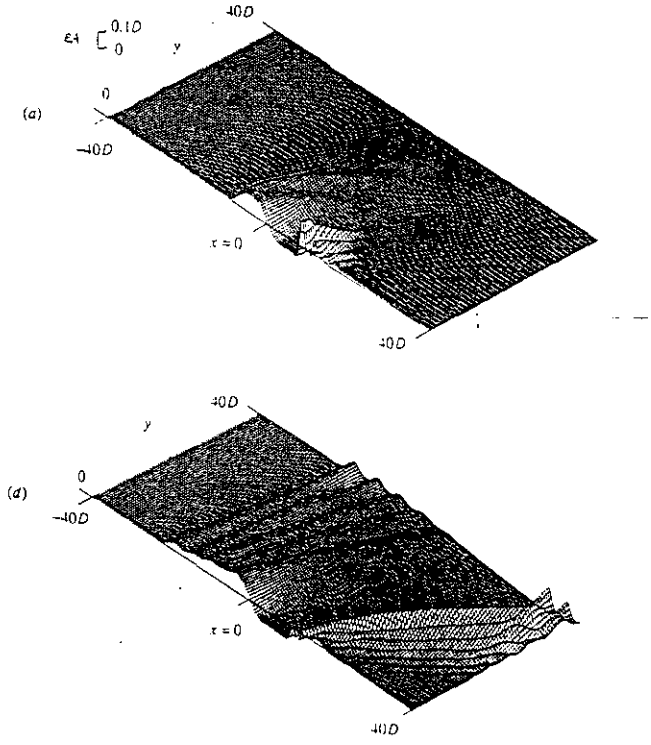

Figure 2. Time development of $A(x,y,t)$ obtained from the solution of the Navier-Stokes equations when F=1.0(two-layer flow). (a) $Ut/D = 40$; (b) $Ut/D = 80$; (c) $Ut/D = 200$; (d) $Ut/D = 400$.

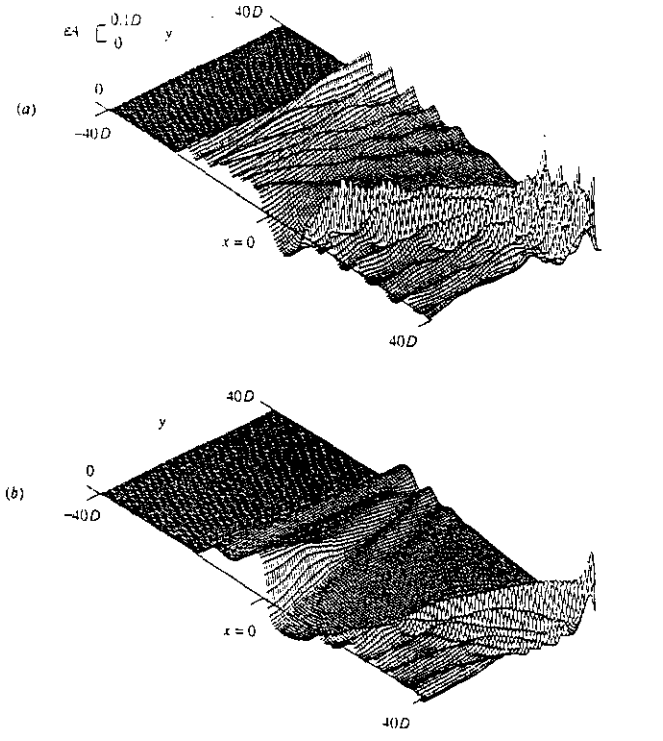

Figure 3. $A(x,y,t)$ obtained from the solution of the weakly nonlinear equations when F=1.0 (two-layer flow, $Ut/D = 200$). (a)fKP equation; (b) fEKP equation.

Experimental study on the three dimensional spherical convections with the parameters of planetary atmospheres

Contact Person: Yoshi-Yuki Hayashi
Department of Earth and Planetary Physics
University of Tokyo

Research Organization: Yoshihisa Matsuda, Yoshi-Yuki Hayashi, Shin-ichi Takehiro
Masaki Ishiwatari, Masahiro Hosaka
Geophysical Fluid Dynamics group, Division of Meteorology
Department of Earth and Planetary Physics, University of Tokyo

Keywords: spherical convection, general circulation, planetary atmospheres, angular momentum, zonal mean flow, teleconnection patterns, SST anomaly, heating response

1. Background

The grand purpose of our study is to reveal the dynamical structures which underlie the general circulations of the planetary atmospheres. It is aimed to construct a theoretical framework which is useful in describing their circulation characteristics, as tried by Golitsyn[1] since 1960's $\sim$. Our interest in due course is to recognize the atmosphere of the earth (or the climate of the earth) as one of the possible realizations in the physical parameter space observed in the solar system.

One of our procedures in revealing the possible underlying dynamics is to gather and classify atmospheric circulation patterns which might be observed under various values of planetary "external" conditions such as orbital parameters (amount and variation of the incoming solar flux), radius and rotation rate of the planet, radiation property of the atmosphere, and surface boundary setups. The sampling of the possible atmospheric circulations is partly possible by numerical experiments by the use of the super computer powers.

Our search in circulation patterns is now performed for the following three major targets:

1. to reveal the possible circulations which might be realized with the earth's condition, but with strongly simplified surface and/or physical processes,
2. to reveal the possible circulations which might be realized with the values of solar flux and orbital parameters which are related to Mars, Earth and Venus,
3. to reveal the possible circulations which might be realized as convection of a spherical shell in general.

The first target includes so called aqua-planet experiment, where all the surface is assumed to be covered by the ocean[2,3]. The aim is to answer the basic problem of the climate, that is, "where and how does it rain?". In the aqua-planet experiments performed so far, the focus has been placed on expecially in searching for the idealistic precipitation distribution of the tropics. The experiment performed here is also in this category, however, the new feature is to find out the deformation of the precipitation distribution to a warm SST (sea surface temperature) anomaly place in the tropics. The configuration is supposed to extract the effect of the existence warm SST region of the real Western Pacific on the general circulation patterns.

The second target is the three dimensional calculations of the so called runaway greenhouse effect. It has been argued, in relation to the evolution of the atmospheres of Venus, Earth and Mars, that there exists a limit of radiation which can be emitted from the top of the atmosphere with the ocean[4]. The interesting point is that the radiation limit is not far from the value of the incoming solar flux of the present earth. It is about 300 W/m^2. The argument placed so far is presented by the use of one dimensional models. It is of interest to observe with three dimensional model to what extent the climate of present earth is stable to the variation of the solar constant. The present concern is to assess the calculation possibility of the evaporation or the freezing of the oceans.

The third target is to refine the dynamical framework of the rotating spherical convection theory, and also to acquire the description ability of the circulation patterns of the deep "atmospheres" as those of outer planets and the sun. The theory of convection in rotating spherical shells has been intensely considered by Busse and his colleagues[4]. The difficulty in their work is that the description utilized is too much mathematical, and hence it is not easy to acquire physical insight. Especially for the distribution of the angular momentum, there has not been presented any satisfactory mechanistic description.

2. Aqua planet experiments with SST anomaly

2.1 Experimental design

The model utilized is basically the same as that used in [3]. It is the three dimensional hydrostatic system on a sphere with very crude physical processes. The dynamical part is represented by the pseudo spectral method with the triangular truncation at wavenumber 42 (T42) and 16 vertical levels. The cumulus parameterizations are Kuo or adjustment scheme. The vertical diffusion is represented by Yamada-Meller Level II scheme. The surface fluxes are evaluated by the usual bulk formula. The radiation processes include

four bands, which are very roughly tuned to give the mean temperature structure resembling the real atmosphere.

The surface is all covered by the ocean (aquaplanet). Note that in the experiments described in this section the value of SST is fixed. The SST distribution for the control experiment is zonally uniform and symmetric about the equator, and has its peak value at the equator. The anomalous SST region is an elliptical area with diameters of 60° in the longitudinal direction wide and 20° in the latitudinal direction wide , which is placed at the equator. The SST is increased by +2K uniformly.

The integrations are performed for 200 days, and the data after 100 days from the initial date are subjected for analyses.

2.2 Precipitation patterns

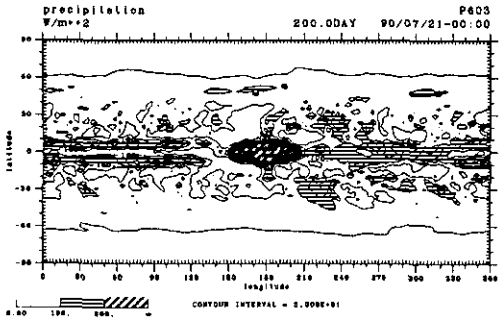

Figure 1

Figure 1 shows the precipitation patterns obtained by the anomalous SST experiment with Kuo cumulus parameterization. Note that the unit is W/m^2. It is obviously observed that in the west of the SST anomaly precipitation is substantially suppressed for about 30° longitudinal width. In the east of the anomaly, the double ITCZ structure, which is one of the characteristics of the precipitation behavior under the control condition, is destroyed. The precipitation peak tends to appear at the equator. In the subtropical regions, the amount of precipitation decreases in the west of the anomaly, while it is increased in the east of the anomaly. Those anomalous characteristics in the precipitation field are also observed with the adjustment parameterization experiments, except for the appearance of the equatorial peak in the east of the anomaly. This is because, with the adjustment scheme, this model tends to have the precipitation peak at the equator.

Corresponding to the asymmetric distribution of the precipitation field, the evaporation field has also a similar asymmetry (not shown). This is caused by the surface wind distribution anomaly, which is caused by the condensation heating due to the precipitation over the anomalous SST region.

2.3 Circulation anomaly

The circulation anomaly can be observed more clearly in the upper tropospheric field. Figure 2 is the anomalous geopotential field (deviation from the zonal mean) at the upper troposphere. It is shown that Rossby wave like patterns are expanding from the increased equatorial SST region to the higher latitudes. The interesting point is that the influence is coming back to the equator at the other side of the hemisphere (180° away from the SST peak).

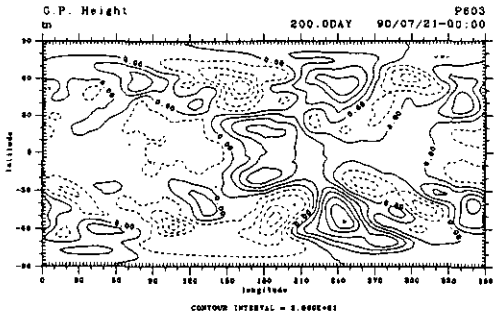

Figure 2

2.4 Acceleration of zonal mean flow

Figure 3 shows the mean zonal wind fields for the control experiment (upper figure) and the SST anomaly experiment (lower figure). We have to note that for the control experiment only the easterly wind region exists in the equatorial region, while for the anomaly experiment, the westerly wind region appears. That is to say, the atmosphere is rotating faster than the solid earth.

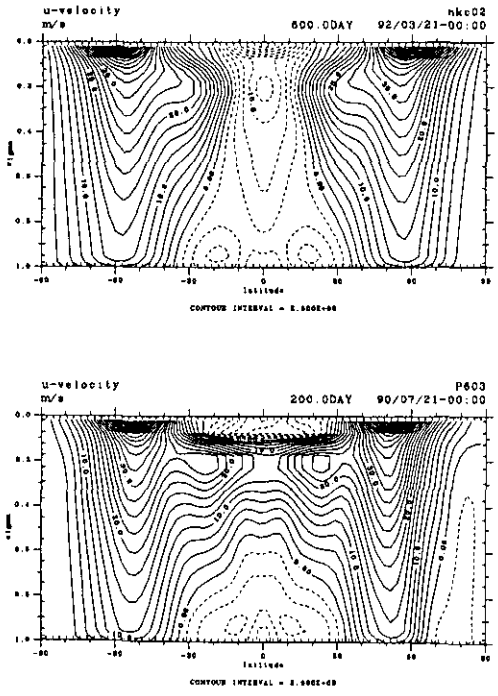

Figure 3

The reason for the momentum accumulation at the equator is considered to be the existence of radiating waves as shown in Figure 2. It seems, although

we have not performed enough dynamical analyses yet, that those wave patterns are due to Rossby waves generating at the heating region and propagating to the higher latitudes. Since the Rossby waves have the easterly momentum, the radiation of Rossby waves from the equatorial region means the westerly acceleration there. Once the equatorial region becomes westerly region, then the radiation of Rossby waves occurs more efficiently, which enhances further acceleration of westerly winds.

3. Aqua planet experiments for runaway greenhouse condition

3.1 Experimental design

The model utilized is basically the same as that used in the previous section. It is the three dimensional hydrostatic system on a sphere with very crude physical processes. The dynamical part is represented by the pseud spectral method with the triangular truncation at wavenumber 21 (T21) and 16 vertical levels. Note that the horizontal resolution is reduced in order to integrate for the longer period in order to trace the evolution of the thermal structure. The cumulus parameterization is so called large scale condensation only. This is because we do not have almost any knowledge on the form of precipitation around the runaway greenhouse situation. We just decide to use the simplest one. The vertical diffusion and the surface fluxes are evaluated by the same scheme as the previous section.

The radiation processes utilized is the exactly same thing as that of [4]. There is no scattering. Only the water vapor absorb the long wave radiation and the absorption coefficient is gray. The sun is assumed to be at the equinox position. hence the zonal mean incoming solar flux is symmetric at the equator.

The surface is all covered by the ocean (aqua-planet). But in this section, the SST is not fixed. The surface does not have heat capacity. The radiation flux, sensible flux, and latent flux are in balance at the surface at any time. This is the so called swamp condition.

Four integrations are performed for 500 days. The first one is started from an isothermal ($T = 280$K) atmosphere with no motion. The solar constant is fixed to be 1360W/m^2. Then after 500 days, the solar constant is increased to 1600 W/m^2. Again the system is integrated for 500 days. And then the solar constant is increased to 1800 W/m^2 and the system is integrated for another 500 days. Finally the solar constant is increased to 2600 W/m^2, which is the value at the orbit of Venus.

3.2 Evolution of global mean temperature and OLR

The evolution of the global mean temperature and OLR (outgoing longwave radiation) is shown in Figures 4, 5 and 6. They are the evolutions for the solar constant of 1360 W/m^2, 1600 W/m^2, 1800 W/m^2, respectively. In each figure, the upper panel represents the temperature evolution while the lower panel represents the OLR evolution. In Figure 4, where the solar constant is at the present earth's value, the temperature and OLR increase initially and approach almost steady final value.

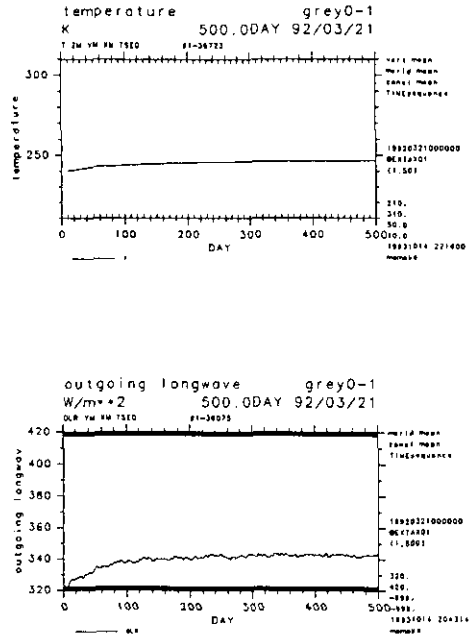

Figure 4

In Figure 5, where the solar constant is increased moderately, the temperature and OLR seem to keep increasing but the tendency is very small and can be expected to reach the steady state.

The funny phenomena can be seen in Figure 5. After the initial slight increase, the OLR begins to decrease and keep going down. The temperature on the other hand keep increasing steadily. This is considered to be the three dimensional realization of the runaway greenhouse effect. The situation can be understood clearly with Figure 6, where the global mean long wave heating rates (K/s) are plotted. Note the value is negative. They are actually the cooling rates. In Figure 6, the dashed line corresponds to the Figure 5 case where the solar constant is 1800 W/m^2, while the solid line corresponds to the Figure 4 case where the solar constant is 1360 W/m^2. It is shown that for 1800 W/m^2 case, the radiative cooling occurs at the higher levels of the atmosphere. This is because the increase of the solar constant causes the increase of atmospheric opacity, which means that the emission from the atmosphere to the space occurs at the higher altitude. If the increase of the emission level is faster and the decrease of the temperature at the emission level is faster than the increase of the global mean temperature, the result turns out to be as shown in Figure 6.

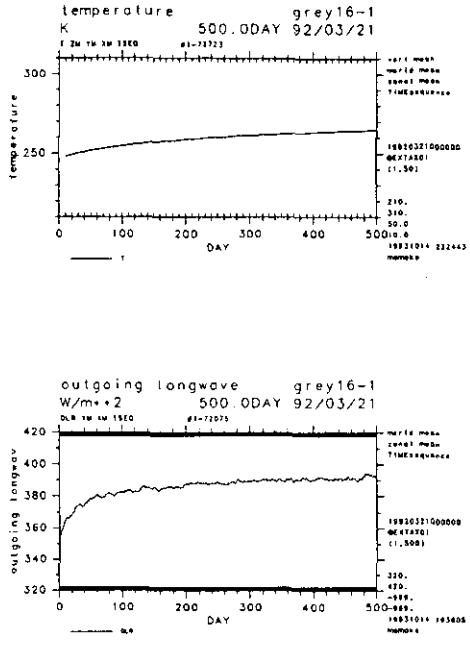

Figure 5

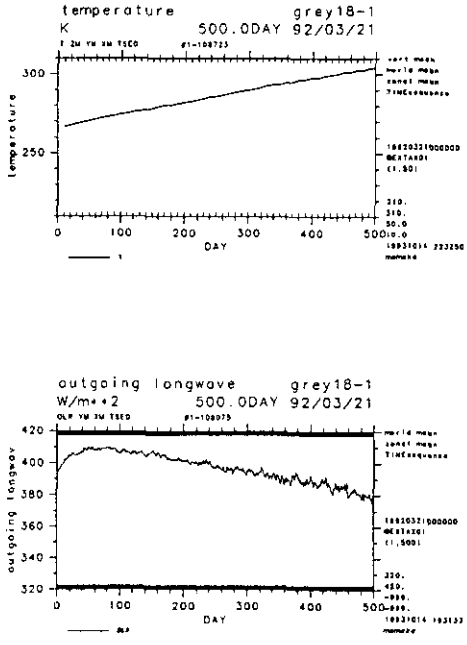

Figure 6

3.3 Acceleration of zonal mean flow

An interesting circulation feature is found in the zonal mean flow field. Figure 8 shows the zonal mean wind for the solar constant of 1360 W/m^2 case (upper panel) and 2600 W/m^2 case. There appears very fast westerly wind (more than 100 m/s) region. Note that in the lower panel, because of the fault of contour routines, contours less than 10 m/s are not drawn.

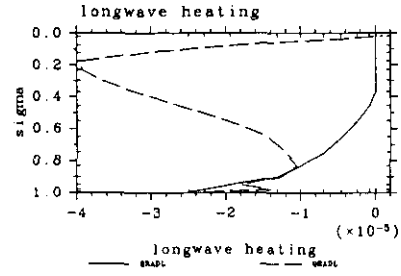

Figure 7

The reason for accumulating such a large amount of super rotating angular momentum is unknown. There is a possibility that numerical problems emerge into the results at this value of solar constant. However, since other fields such as temperature are consistently changing, the result shown in Figure 8 might pick up a new dynamical regime. Actually, zonal mean profile of the condensation heating has peak vale not at the equator but in the mid latitudes. The circulation is downward at the equator. The mean circulation is completely different from the ordinary circulation of the present atmosphere. We have to produce wave activity diagnosis, to perform two dimensional zonally symmetric calculations, and so on, before having further discussion on this matter.

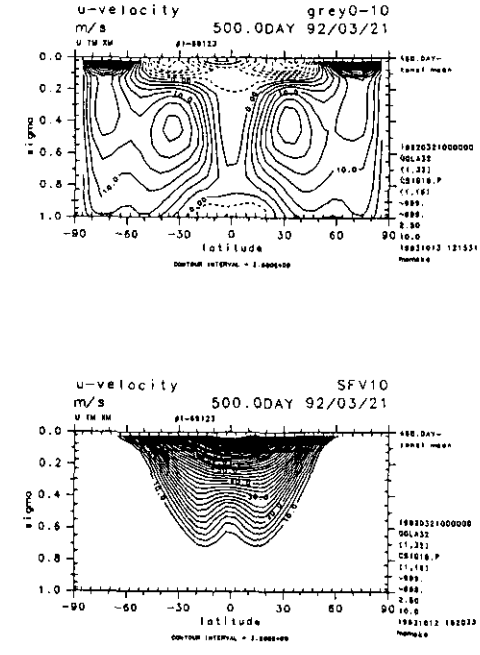

Figure 8

4. Boussinesq convection in a spherical rotating shell.

4.1 Experimental design

In order to reinforce the knowledge of formation of zonal mean flows, we start from a reconsideration of the zonal mean flow distributions induced by Boussinesq convection in a spherical rotating shell. This is the typical starting point of the thorough theoretical consideration. To start with the consideration is limited to the cases where rotation rate is small. The conditions considered include homogeneous internal heat sources and fixed temperature boundaries as the thermal conditions, and free-slip boundaries as the kinematic conditions. This is a standard set of boundary conditions in the sense that many investigations have been performed already. However, the classification of momentum redistribution is not considered so far.

The calculation performed here just follows the weak nonlinear procedure. The linear critical modes are numerically calculated by solving the linear stability problem. Then the zonal mean flows which equilibrate the acceleration due to the nonlinear forcing caused by the linear critical modes are also numerically calculated.

4.2 Zonal mean flow acceleration

The calculated distribution of mean zonal flows are shown in Figure 9. Figure 9a is the result for Taylor number $Ta = 10$. The ratio of the inner radius to the outer radius is $\eta = 0.6$. Prandtle number is $Pr = 1$. Note that the westerly (super rotating) region appears at the equatorial region.

Figure 9b is the case where Prandtle number is increased ($Pr = 100$) from that of Figure 9a. All the other parameters are fixed. Note that easterly region appears at the equator. Figure 9c is the case where the inner radius is decreased, i.e., the convective layer depth is increased from that of Figure 9a. All the other parameters are fixed. This case also show the easterly wind region at the equator. It seems that a transition from equatorial super rotation to retrograde rotation occurs as the value of Prandtl number and/or the thickness of spherical shells increase.

This tendency can be understood by the variation of relative importance of the transports of angular momentum between by mean meridional circulations $\langle \Omega \overline{v} r \cos^2 \phi \rangle$ and by Reynolds stresses $\langle \overline{uv} \cos \phi \rangle$. The total angular momentum transport is described by

$$\frac{\partial}{\partial t} \langle \overline{u} r \cos \phi \rangle + \frac{1}{\cos \phi} \frac{\partial}{\partial \phi} \left[\cos \phi \left(\langle \Omega \overline{v} r \cos^2 \phi \rangle + \langle \overline{uv} \cos \phi \rangle \right) \right] = \langle F_\lambda r \cos \phi \rangle,$$

where r is radius, ϕ is longitude, u, v is eastward and northward wind, $\langle\rangle$ is vertical mean, $\overline{()}$ is zonal mean, F_λ is frictional diffusion term.

The Reynolds stress due to convective cell causes westerly acceleration, because $\overline{uv}$ becomes equatorward owing to the Coriolis effect. On the other hand, since the mean meridional circulation is from equator to pole in the outer region while pole to equator in the lower region, the mean transfer of angular momentum due to mean meridional circulation causes easterly acceleration. Since Prandtle number becomes large, that is, friction is increased, the velocity correlation due to Coriolis effect becomes small and thus easterly acceleration occurs. Similarly, if the radius of the inner sphere becomes small, the mean meridional circulation transport the momentum to the higher latitudes more efficiently, and again, eastward acceleration occurs.

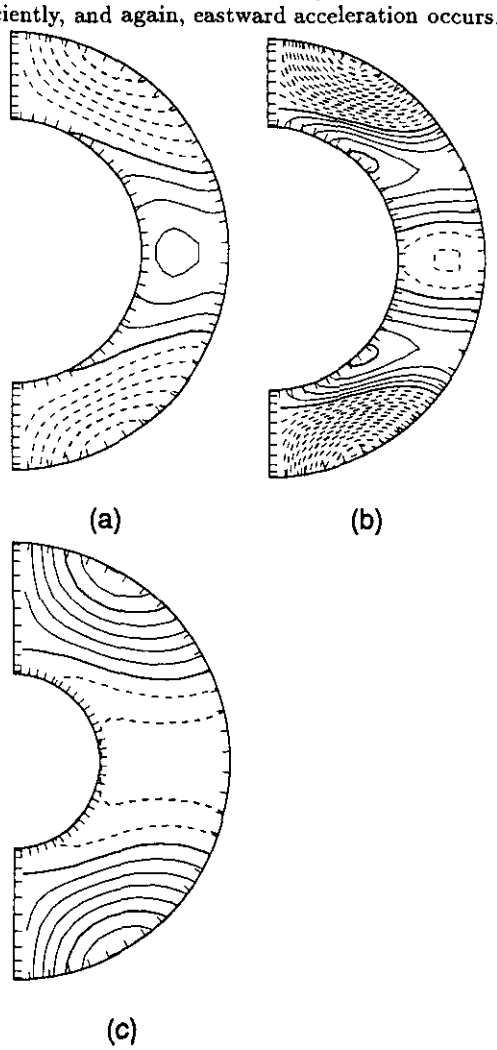

Figure 9

Acknowledgement

We wish to thank Drs Mitsumoto, Numaguti, and other NIES staff members for providing us with this powerful computing facility. A number of suggestions and supports by Dr. Numaguti on softwares, hardware usages, and sciences were indispensable to our research performance. Our software environment was provided from the resources of GFD DENNOU CLUB. GFD DENNOU CLUB is an independent group of scientists aiming at collecting basic software resources for research and education of geophysical fluid dynamics and related fields. Those resources include three di-

mensional spherical primitive system originally developed by Dr. Numaguti while he was at University of Tokyo. We also have to express our thanks to the staffs of TISN (Tokyo university International Science Network) in providing us with data connection between NIES and University of Tokyo.

References

1. G.S. Golitsyn, *ICARUS*, **13**, 1 (1970)
2. Y.-Y. Hayashi and A. Sumi, *J. Met. Soc. Japan*, **64**, 451 (1986)
3. A. Numaguti and Y.-Y. Hayashi, *J. Met. Soc. Japan*, **69**, 541 (1991)
4. S. Nakajima, Y.-Y. Hayashi and Y. Abe, *J. Atmos. Sci.*, **49**, 2256 (1992)
5. K.-K. Zhang and F.H. Busse, *Geophys. Astrophys. Fluid Dynamics.*, **39**, 119 (1987)

Baroclinic instability of Kirchhoff's elliptic vortex

Contact Person

Takeshi Miyazaki
Department of Mechanical and Control Engineering,
University of Electro-Communications.

Research Organization

Hideshi Hanazaki
Division of Atmospheric Environment, National Institute for Environmental Studies,
Environment Agency of Japan.
Weiming Sha
Department of Mechanical and Control Engineering, University of Electro-Communications.

Keywords

Kirchhoff's elliptic vortex, baroclinic instability, quasi-geostrophic approximation

1. Introduction

Concentrated vorticity region often appears as a coherent structure in geophysical flows, where the fluid motions are subject to a strong influence both of the Coriolis force and the density inhomogeneity associated with temperature and/or salinity variations. Vertical vortices (here, those with vertical vorticity component are meant), such as the "Meddies" in the ocean, keep their identity for a very long time. The motion and stability of these vortices embedded in a stratified rotating fluid is an important subject for the understanding of the physical mechanisms of energy and momentum transport in geophysical flows.

Geophysical fluid motions are often well described by a quasi-geostrophic approximation and many investigations on vortex instability have been performed based on the quasi-geostrophic, f-plane equations. For instance, Flierl[1] solved the normal-mode equations analytically for a class of isolated model vortices with piecewise-constant vorticity. He showed that a "baroclinic" instability mode becomes more unstable than barotropic modes, if the scale of the whole vortex is small compared to the radius of deformation. Similarly, Gent & McWilliams[2] and Carton & McWilliams[3] solved numerically the normal-modes equations for several continuous vorticity profiles. They reported that the fastest growing perturbation is often "baroclinic" (they called it an internal instability). The "baroclinic" instability is called, sometimes, the "internal barotropic" instability, but we follow the terminology of Flierl throughout this paper.

We consider the linear stability of an elliptic vortex patch in this paper. Specifically, we consider the Kirchhoff's elliptic vortex, a vortex patch with uniform vorticity (unity without loss of generality) inside of an ellipse whose major and minor semi-axes are a and b. If it is embedded in an irrotational fluid, it rotates solidly with a constant angular velocity $W=ab/(a+b)^2$. Love[4] studied the linear barotropic stability of the Kirchhoff's elliptic vortex and showed that it becomes unstable to disturbance with azimuthal wave number 3, if the ratio a/b is greater than 3. Our objective is to clarify the baroclinic effects on the stability of Kirchhoff's ellipse.

2. Formulation

The quasi-geostrophic equations of motion (conservation of the potential vorticity) on the f-plane are written in terms of a streamfunction y, as

$$\left[\frac{\partial}{\partial t}+\frac{\partial\psi}{\partial y}\frac{\partial}{\partial x}-\frac{\partial\psi}{\partial x}\frac{\partial}{\partial y}\right][\Delta+L_z]\psi=0. \qquad (1)$$

Here, D denotes the Laplacian operator in the horizontal plane and L_z is a differential operator representing the effect of stratification. The explicit form of L_z is not required in the following stability analysis. The streamfunction inside of the Kirchhoff's elliptic vortex is given by,

$$\Psi_{in}=-\frac{bx^2+ay^2}{2(a+b)}, \qquad (2)$$

where the uniform (relative) vorticity in the interior of the ellipse is taken to be unity and a is the major semi-axis and b is the minor semi-axis. The Kirchhoff's elliptic vortex rotates rigidly about the z-axis with a constant angular velocity

$$\Omega=\frac{ab}{(a+b)^2}. \qquad (3)$$

The elliptic-cylinder coordinates (x, h, z) are convenient in describing the geometry of the basic flow field:

$$x=c\cosh\xi\cos\eta,$$
$$y=c\sinh\xi\sin\eta,\ 0\le\eta\le2\pi \qquad (4a,b)$$

where $c=\sqrt{a^2-b^2}$. In these coordinates, the boundary of the elliptic vortex is re-presented by

$$\xi=\xi_0=\frac{1}{2}\log\left(\frac{a+b}{a-b}\right), \qquad (5)$$

and the streamfunction outside of the vortex is written as

$$\Psi_{out}=-\frac{ab}{2}\xi-\frac{ab}{4}e^{-2\xi}\cos2\eta. \qquad (6)$$

Since the basic flow is uniform in the vertical direction, we can introduce the normal-mode disturbances of the form

$$\psi_{in,out}=\Psi_{in,out}+\varepsilon f(z)\hat{\psi}_{in,out}(\xi,\eta)e^{-i\omega t},$$
$$(\varepsilon<<1) \qquad (7)$$

where f(z) denotes the eigenfunction of a Sturm-Liouville problem associated with the differential

operator L_z. With appropriate boundary conditions, f(z) corresponds to the eigenvalue l by

$$L_z f(z) = -l^2 f(z) . \tag{8}$$

The boundary of the vortex patch is assumed to deform as

$$\xi = \xi_0 + \varepsilon F(\eta) f(z) e^{-i\omega t} . \tag{9}$$

The disturbance streamfunctions (both inside and outside of the ellipse) obey the Helmholtz equation:

$$(\Delta - \lambda^2)\hat{\psi}_{in,out} = 0,$$
$$\left(\left[\frac{\partial^2}{\partial\xi^2} + \frac{\partial^2}{\partial\eta^2} - 2q(\cosh 2\xi - \cos 2\eta)\right]\right) \hat{\psi}_{in,out} = 0$$
$$\text{with } q = \frac{1}{4}c^2\lambda^2). \tag{10a,b}$$

At O(e), the kinematical boundary conditions that the boundary of the vortex patch continues to be the boundary are written, on $x=x_0$, as

$$i\omega h^2 F + \frac{\partial\hat{\psi}_{in}}{\partial\eta} - \Omega\frac{\partial}{\partial\eta}(h^2 F) = 0,$$
$$i\omega h^2 F + \frac{\partial\hat{\psi}_{out}}{\partial\eta} - \Omega\frac{\partial}{\partial\eta}(h^2 F) = 0, \tag{11a,b}$$

where h^2 denotes the metric factor, i.e.,

$$h^2 = \frac{1}{2}c^2(\cosh 2\xi - \cos 2\eta) . \tag{12}$$

The dynamical condition on $x=x_0$ is the continuity of tangential velocity, which is identical to the condition of pressure continuity:

$$\frac{\partial\hat{\psi}_{in}}{\partial\xi} - \frac{\partial\hat{\psi}_{out}}{\partial\xi} = h^2 F. \tag{13}$$

The solutions of (10a,b) are expanded in terms of the Mathieu functions (truncated at N=30), and the problem is reduced to an eigenvalue problem of a 2Nx2N matrix. The eigenvalues w and the eigenvectors are calculated numerically using the QR method.

3. Results

Since the odd (2p-periodic) and even (p-periodic) modes are decoupled completely, we will describe the results for the odd modes and those for the even modes separately.

Figure 1 shows the contours of constant growth-rate of the odd modes in the l-a/b plane, where the horizontal axis is the vertical wave number l and the vertical axis is the aspect ratio a/b and the contour interval is 0.01. It is remarkable that the Kirchhoff's elliptic vortex is unstable to the bending mode (m=1) irrespective of a/b for certain range of l and that the unstable region touches the l-axis at $l = l_c = 1.7046$. Close examination shows that the growth-rate of the bending mode is proportional to a/b-1, when it is very small. The perturbed vortex boundary and the disturbance streamfunction for a/b=2.0 and l=1.25 are shown in Figs. 2a and b, respectively. We can see clearly that the instability mode has an azimuthal wave number 1 and a phase shift of about p/4 (to the major semi-axis). This instability occurs as the result of resonant interaction between the baroclinic bending wave and the barotropic elliptical deformation wave (see for details Miyazaki & Hanazaki[5]).

As for even modes, Fig. 3 depicts the contours of constant growth-rate in the l-a/b plane. Only the m=2 mode appears in the parameter region described in this figure (a/b<4). The shape of the deformed vortex patch and the perturbation streamfunction are illustrated in Figs. 4a,b (a/b=2.0, l=0.5). Any ellipse is unstable to the m=2 baroclinic mode irrespective of the value of a/b. The growth rate increases and the unstable l-range becomes wider as the ratio a/b increases. Close examination shows that the growth-rate decays like $(a/b-1)^2$ in the limit $a/b \to 1$. The physical mechanism of this instability seems to be related to a side-band instability (Benjamin-Feir instability) of finite-amplitude barotropic waves.

Using Figs.1 and 3, we can judge whether an ellipse of a given aspect ratio a/b is stable or unstable, if the spectrum $\{l_n\}$ of the Sturm-Liouville problem (8) is known.

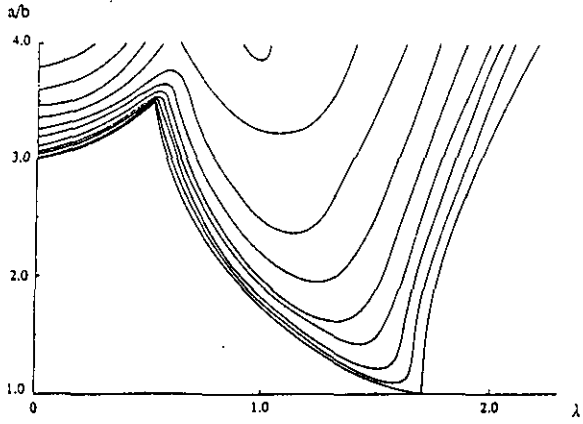

Fig.1 The contours of constant growth-rate of the odd modes in the λ-a/b plane

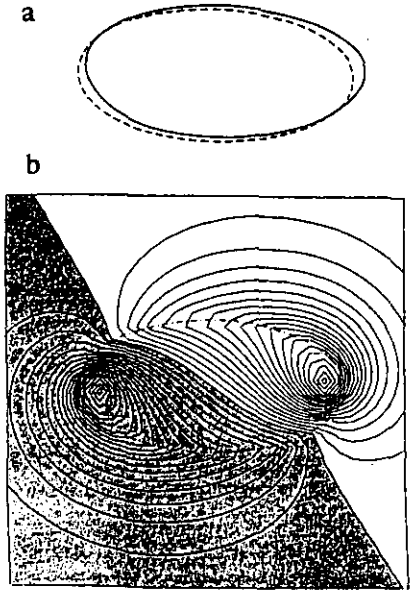

Figs.2a,b The perturbed vortex boundary and the disturbance streamfunction for a/b=2.0 and λ=1.25

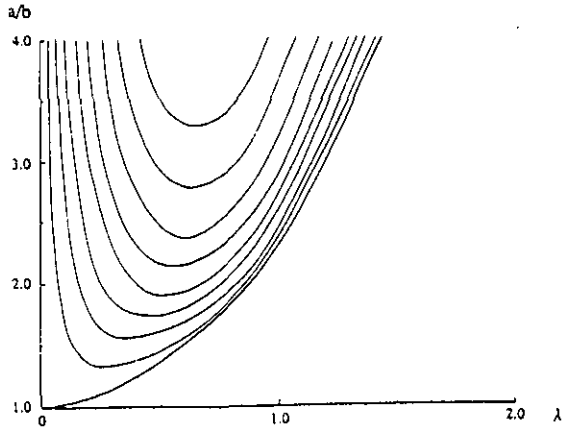

Fig.3 The contours of constant growth-rate of the even modes in the λ-a/b plane

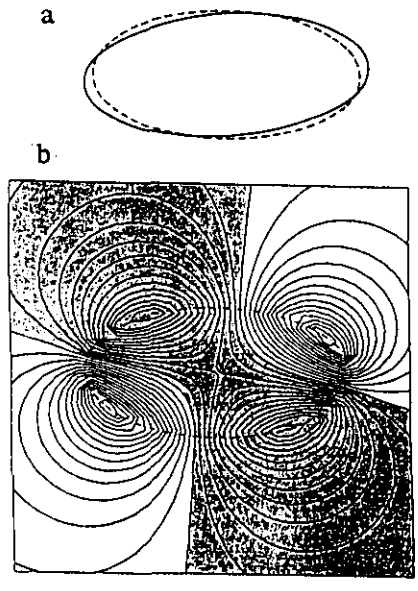

Figs.4a,b The perturbed vortex boundary and the disturbance streamfunction for a/b=2.0 and λ=0.5

Acknowledgments

We are grateful to Dr. Y. Fukumoto for valuable comments and discussions during this study. We owe much to K. Hirahara in preparing figures.

References

1. G.R.Flierl, *J. Fluid Mech.* **197**, 349-388 (1988)
2. P.R.Gent and J.C.McWilliams, *Geophys. Astrophys. Fluid Dyn.* **35**, 209-233 (1986)
3. X.J.Carton and J.C.McWilliams, *"Mesoscale/Synoptic Coherent Structures in Geo-physical Turbulence"*, *Elsevier* (1989), 225-244
4. A.E.H. Love, *Proc. London Math. Soc.* **25**, 18-42 (1893)
5. T.Miyazaki and H.Hanazaki, *J. Fluid Mech.* in press (1993)

Time Spectral Analysis for the Natural Variability of the Barotropic Model Atmosphere

H. L. Tanaka and Kazuo Kimura
Institute of Geoscience
University of Tsukuba, Japan

Keywords: climate model, climate change, natural variability, time spectrum

1 Scientific Background

Climate variation in nature is composed of two components: one is caused by unusual external forcing and the other is the inherent natural variability which occurs even under the fixed boundary conditions. A detailed analysis of climate variability is an important research subject to understand the issue in the global change. Occurrence of short term abnormal weather may be regarded as a signal of the climate variation superimposed on the natural variation.

Recent global warming is anticipated to have been caused mostly by the increased CO_2, which acts as the external forcing of the atmosphere. It is important to know the quantitative magnitude of the recent warming induced by the greenhouse gases such as CO_2. If the anticipated warming is caused mostly by these greenhouse gases, some immediate political action has to be taken to reduce the greenhouse gases. However, if the recent warming is just due to the natural trend or natural variability of the chaotic atmosphere which has no relation to the increased greenhouse gases, there is no need to worry about the release of these greenhouse gases into the atmosphere. Therefore, the first step to assess the recent climate variation is to separate the variability into the forced trend due to the increased greenhouse gases and a natural variability of the atmosphere superimposed on the forced trend.

Atmospheric general circulation models under fixed boundary conditions, such as the fixed sea surface temperature (SST), indicate their own natural variability determined by the characteristic physical processes included in the models. Likewise, coupled atmosphere-ocean models and more complicated climate system models would indicate their own natural variability under the fixed wider class of the boundary conditions, such as the type of gas constituent and astronomical parameters. The process to determine the magnitude of the natural variability depends highly on the complexity of the model. However, it is not clear how the natural variability depends on the complexity and the internal nonlinear structure of the model. Even a simple barotropic model with an energy source and sink can show its characteristic natural variability. Hence, it is an interesting subject to evaluate the magnitude of the natural variability for different climate models and find some rules between the model complexity and the induced natural variability.

2 Objective

The objective of this study is to find the typical magnitude of the natural variability of a model atmosphere by a long term integration (1000 years) of a simple barotropic model under a fixed boundary condition. The results will be compared with the natural variability of other climate models.

3 Model description

A 3-D spectral representation of primitive equations may be written by the following general form after a suitable diagonalization of the linear terms:

$$\frac{dw_i}{d\tau} + i\sigma_i w_i = -i\sum_{jk} r_{ijk} w_j w_k + f_i, \quad i = 1,2,3,...$$

where w_i and f_i represent the spectral expansion coefficients of the dependent variables and external forcing, respectively. The symbol σ_i denotes the eigenfrequency of the normal mode in a resting atmosphere, and r_{ijk} is the interaction coefficient for nonlinear wave-wave interactions.

In the 3-D spectral representation, the vertical expansion basis functions may be divided in barotropic and baroclinic components. In this study, we attempt to construct a spectral barotropic model, using only the barotropic components of w_i. The spectral equation for such a barotropic model has the same form as for the baroclinic model, except the fact that the barotropic-baroclinic interactions should be included formally in f_i.

In this study, we consider the next forcing:

$$f_i = (BC)_i + (DF)_i + (ZS)_i + (VP)_i,$$

where $(BC)_i$ represents the baroclinic instability, $(DF)_i$ the biharmonic diffusion, $(ZS)_i$ the zonal surface stress, and $(VP)_i$ the vertical propagation of planetary waves. The unique energy source of the model is $(BC)_i$, and the rest of the three physical processes are the energy sinks in this model. The nonlinear interaction is designated as $(NL)_i$. Refer to Tanaka (1991) for the detail of the model description.

4 Results

We integrated the simple spectral barotropic model for 1000 years under a fixed boundary condition. Figure 1a to 1d illustrate the time series of the total energy of the model atmosphere for 1, 10, 100, and 1000 years, respectively. The model output is stored for every 24 hours. Those time series in Figs 1 are the plots for daily value, 10-day, 100-day, and 1000-day averages, respectively. Namely, every panel of the time series contains 365 points of data.

Figure 1a shows a smooth variation of energy level starting from about 11 $\times$ 10^5 Jm^{-2}. The energy increases to 17 $\times$ 10^5 Jm^{-2} after about 20 days and has reached to an equilibrium, fluctuating the mean level. This time series seems to contain a low-frequency variability with a period of approximately 50 days.

Figure 1b is the time series of the 10-day mean of the same energy variation for 10 years. We can see the initial increase at the first 20 days at the left-most edge of the time series. The energy level varies within a range from 14 to 22 $\times$ 10^5 Jm^{-2}. This range characterizes the magnitude of the natural variability of the model atmosphere.

Figure 1c is for the 100-day mean time series during 100 years. Since the 100-day mean filters out most of the dominant oscillations, the range of the natural variability is reduced substantially compared with the 10-day mean time series in Fig. 1b. Similarly, Fig. 1d is for the 1000-day mean time series during 1000 year integration period. The range of the natural variation has reduced in this plot to about 1 $\times$ 10^5 Jm^{-2}. This time series differs substantially from that of Fig.1a in its characteristics of variation. We find practically no ultra-low-frequency variability at this time scale beyond the 50 day period.

Figure 2 illustrates the power spectrum of the time series of the total energy for the 1000-year integration. The power spectrum is estimated by the FFT routines and is smoothed by averaging 64 term of the original power spectrum. The frequency resolution of the spectrum is about 1/(10-years) which is still fine enough to argue the detailed spectral properties.

The result clearly separates the two characteristic spectral slopes of the model atmosphere. It is obvious that the spectrum is white for the period beyond 50 days. In other word, the random variable has no memory of the past for the variation beyond the 50-day period. In contrast, the spectrum is red for the period shorter than 50 days. Namely, the random variable remembers its own past to some extent for the variation shorter than 50-day period. Interestingly, the spectral slope for the red noise obeys approximately the -3 power of the frequency. There is an energy source into the system at the frequency range near 1/(5-day) due to the parameterized baroclinic instability. Separated by this energy source, the spectral slope appears to change to -4 power of the frequency at the higher frequency range over 1/(5-day) to 1/(2-day).

The red noise spectrum extends over the range from 1/(50-day) to 1/(2-day). Although there is no apparent spectral peak near the frequency at 1/(50-day), we can observe the dominant variation with the time scale of about 50 days as in Fig. 1a due to the fact of the dominant spectral power at this range relative to the higher frequency range of the red noise.

Figure 1

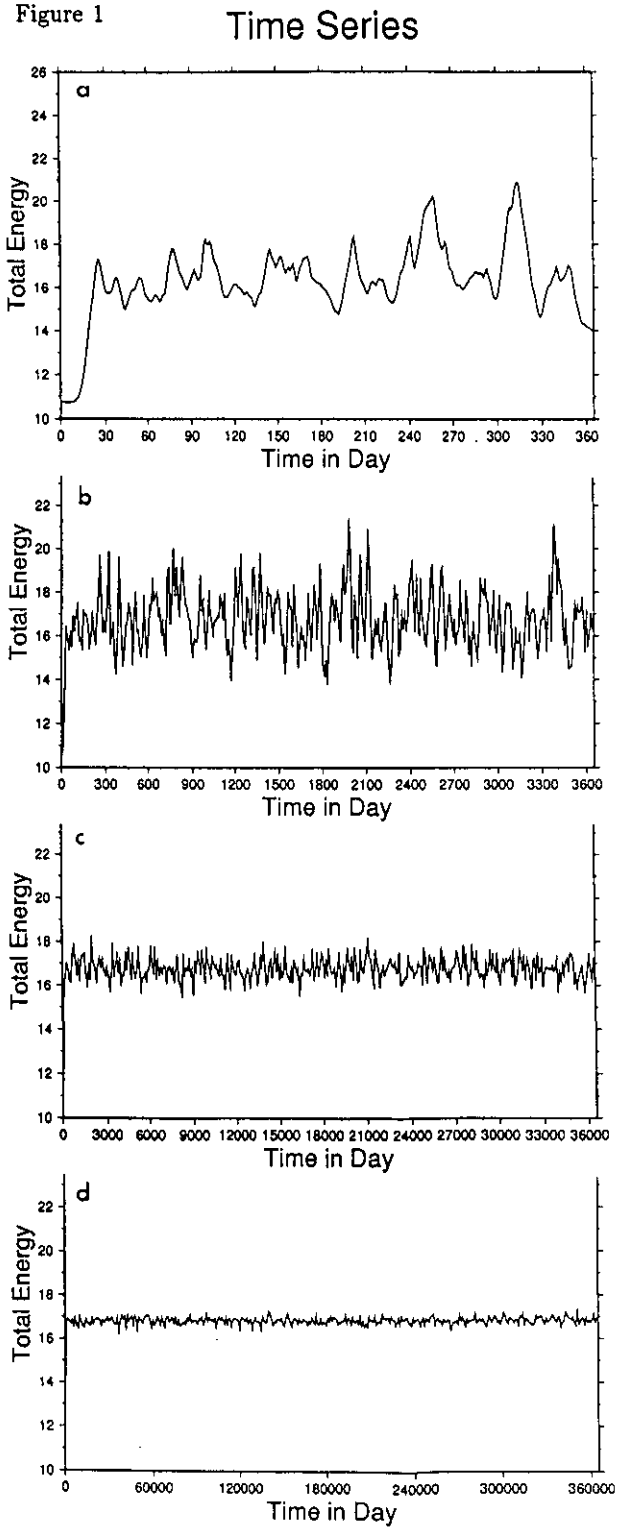

5 Summary

The results of the 1000 year time integration of a simple barotropic model with an energy source from the parameterized baroclinic instability are summarized as the following three points:

1. The total energy of the model atmosphere shows natural variation in the range from 14-22 $\times$ 10^5 Jm^{-2} for the long-term average of 17 $\times$ 10^5 Jm^{-2}.
2. The time spectrum of the model atmosphere is characterized as white noise for the low-frequency variability with its period longer than 50 days. In contrast, the spectrum is characterized as red noise for the period shorter than 50 days.
3. It is found in this study that the red noise spectrum over the spectral range for 1/(50-day) to 1/(5-day) obeys a characteristic -3 power low. Since there is a unique energy source into the system near the frequency at 1/(5-day) in terms of the baroclinic instability of synoptic disturbances, we can expect a reverse energy cascade from higher- to lower-frequency ranges associated with the -3 power law of the power spectrum.

6 Acknowledgments

We appreciate Dr. S. Mitsumoto for his kind arrangement in using the computing facility at the NIES.

7 References

1. H.L. Tanaka, *Mon. Wea. Rev.*, **119**, 2919-2935 (1991)

Figure 2